Influence of energy-dependent particle diffusion on the X-ray spectral curvature of MKN 421

Pranjupriya Goswami, Sunder Sahayanathan, Atreyee Sinha, Ranjeev Misra, Rupjyoti Gogoi

Monthly Notices
of the
ROYAL ASTRONOMICAL SOCIETY

MNRAS **480,** 2046–2053 (2018)
Advance Access publication 2018 July 30

doi:10.1093/mnras/sty2003

Influence of energy-dependent particle diffusion on the X-ray spectral curvature of MKN 421

Pranjupriya Goswami,[1]★ Sunder Sahayanathan,[2] Atreyee Sinha,[3,4] Ranjeev Misra[3] and Rupjyoti Gogoi[1]

[1]*Department of Physics, Tezpur University, Napaam 784028, India*
[2]*Astrophysical Sciences Division, Bhabha Atomic Research Centre, Mumbai 400085, India*
[3]*Inter-University Center for Astronomy and Astrophysics, Post Bag 4, Ganeshkhind, Pune 411007, India*
[4]*APC, AstroParticule et Cosmologie, Université Paris Diderot, CNRS/IN2P3, CEA/Irfu, Observatoire de Paris, Sorbonne Paris Cité, 10, rue Alice Domon et Léonie Duquet, 75205 Paris Cedex 13, France*

Accepted 2018 July 24. Received 2018 July 20; in original form 2018 May 28

ABSTRACT

The X-ray spectral curvature of blazars is traditionally explained by an empirical log-parabola function characterized by three parameters, namely the flux, curvature, and spectral index at a given energy. Since their exact relationship with the underlying physical quantities is unclear, interpreting the physical scenario of the source through these parameters is difficult. To attain an insight on the X-ray spectral shape, we perform a detailed study of the X-ray spectra of the blazar MKN 421, using an analytical model where the electron diffusion from the particle acceleration site is energy dependent. The resultant synchrotron spectrum is again determined by three parameters, namely, the energy index of the escape time-scale, the quantity connecting the electron energy to the observed photon energy, and the normalization. The X-ray observations of MKN 421, during 2012 July–2013 April by *Nuclear Spectroscopic Telescope Array* and *Swift*-XRT are investigated using this model and we find a significant correlation between model parameters and the observational quantities. Additionally, a strong anticorrelation is found between the fit parameters defining the spectral shape, which was not evident from earlier studies using empirical models. This indicates the flux variations in MKN 421 and possibly other blazars, may arise from a definite physical process that needs to be further investigated.

Key words: acceleration of particles – diffusion – galaxies: active – BL Lacertae objects: individual: MKN 421 – X-rays: galaxies.

1 INTRODUCTION

Blazars are an extreme class of Active Galactic Nuclei (AGN) with the relativistic jet aligned towards the observer. Their broad-band spectral energy distribution (SED), extending from radio to γ-ray energies, is characterized by two prominent peaks with the low-energy component attributed to synchrotron emission and the high energy to inverse Compton processes. The spectral modelling of the synchrotron component suggests the underlying electron distribution to be a broken power law with a smooth transition at the break energy corresponding to the peak of the SED (Sambruna et al. 1994; Tavecchio, Maraschi & Ghisellini 1998; Fossati et al. 2000). Alternatively, the spectrum around the peak is well reproduced by a log-parabola function, requiring a lesser number of free parameters (Landau et al. 1986; Massaro et al. 2004a; Tramacere et al. 2007; Paggi et al. 2009; Chen 2014). Recent high-resolution optical–X-ray observations showed that the spectrum deviates from a power law even beyond the synchrotron peak and is better represented by functions with mild curvature (Bhagwan et al. 2014; Gaur et al. 2017). These observational inputs motivate one to look for a modified non-thermal electron distribution capable of explaining the broad-band synchrotron spectra of blazars.

The log-parabola spectral shape of the synchrotron peak was observed to be the best-fitting model for various blazars and during different flux states. This initiated an extensive study of the peak spectral curvature to identify possible correlations between the model parameters and to relate their property to the underlying particle acceleration process (Massaro et al. 2004a,b, 2008; Tramacere et al. 2007). For most of the sources, the curvature parameter is positively correlated with the flux corresponding to peak energy, while no substantial correlation was observed between the curvature parameter and the spectral index at a fixed energy (Ka-

★ E-mail: pranjupriya.g@gmail.com

panadze et al. 2014; Sinha et al. 2015). On the other hand, several studies show a significant positive correlation between the peak energy of the fitted log-parabola function and the corresponding flux (Massaro et al. 2006, 2008; Tramacere et al. 2007; Paggi et al. 2009). The dependence of the peak energy to the corresponding flux can be used to identify the dominant parameter responsible for the spectral change. However, these studies are often performed over a narrow X-ray energy band where a log-parabola function provides a decent fit statistic.

A log-parabola photon spectral shape can originate if the emitting electron distribution is also a log-parabola. Such a distribution can originate from an energy dependence of the acceleration probability, as shown by (Massaro et al. 2004a). Alternatively, the curvature can also be interpreted as a result of the energy dependence of the escape time-scale from the emission region. This model is capable of explaining the broad-band SED with a power-law spectral shape at low energies and a smooth curvature at the high energies (Sinha et al. 2017). On the other hand, an energy dependence of the escape time-scale in the AR is capable of producing a spectrum that deviates from a power law and closely agrees with a broken log-parabola (Jagan et al. 2018).

The blazar MKN 421 is one of the nearest ($z = 0.031$) and the brightest known BL Lac object that has been studied extensively with multi-epoch observations over a wide spectral range (Acciari et al. 2009; Abdo et al. 2011; Aleksić et al. 2012; Bartoli et al. 2016; Sinha et al. 2016). This source is classified as a high frequency BL Lac (HBL) as its synchrotron peak falls at X-ray energies (Padovani & Giommi 1995). The X-ray spectra of this source exhibit significant curvature in both flaring and quiescent states. The high flux state spectra can be well fitted by a log-parabola function (Massaro et al. 2004a, 2006; Donnarumma et al. 2009; Yan et al. 2013; Sinha et al. 2015); whereas, the low flux state spectra are better explained with power law or power law with exponential cut-off models (Yan et al. 2013; Kataoka & Stawarz 2016). Alternatively, Zhu et al. (2016) showed that the X-ray and γ-ray spectra of the source can be reproduced using synchrotron and self-Compton emission models with the underlying electron distribution assumed to be a combination of power law and log-parabola shape. A detailed X-ray spectral study of the source, at energies 0.1–100keV, was performed by Massaro et al. (2004a) using BeppoSAX observations of 1999 May and 2000 April–May. The X-ray spectra can be well fitted by a log-parabola function with the curvature parameter showing a strong positive correlation with the spectral index at 1 keV. However, no such correlation between these model parameters is found in a combined *Swift*-XRT and *Nuclear Spectroscopic Telescope Array (NuSTAR)* spectra of the source during 2013 April (Sinha et al. 2015). Similar to other BL Lac objects, MKN 421 also showed a strong positive correlation between the log-parabola peak energy and the peak flux and a negative correlation between peak energy and the curvature parameter (Massaro et al. 2004b, 2006, 2008; Tramacere et al. 2007, 2009). Interestingly, the flux-to-hardness ratio plot of the source during various flaring episodes show both clockwise or anticlockwise patterns (Tramacere et al. 2009; Kapanadze et al. 2016).

In this work, we analyse *NuSTAR* observations of the blazar MKN 421 during the period 2012 July–2013 April and perform a detailed investigation of the X-ray spectral curvature. Additionally, we supplement this with *Swift*-XRT observation at low energies, thereby enabling a broad-band (0.3–80keV) X-ray study of the source. To gather a better insight into the physics behind the X-ray spectral curvatures, we use a physically motivated model by considering the dynamics of the electrons in the main acceleration zone. The broad-band X-ray spectrum is fitted using this analytical model and the results are presented. Finally, we study the correlations between different model parameters and compare them with the ones obtained from the empirical log-parabola spectral fit.

The paper is organized as follows: In the following section, we describe the details of the data analysis procedure and in Section 2.3, we present our spectral study using the empirical log-parabola model. The details about the analytical model involving the dynamics of the particle acceleration and the spectral fitting are presented in Section 3 along with the correlation studies. Finally, in Section 4 we discuss our results in light of current scenario of the blazar spectral studies.

2 X-RAY OBSERVATION AND ANALYSIS

MKN 421 has been monitored by *NuSTAR* in the hard X-ray energy band during flaring as well as quiescent flux states. The source underwent a strong X-ray flare from 2013 April 10 to 19 and was observed by both *NuSTAR* and *Swift*-XRT, simultaneously. In order to study the spectral behaviour of the source during different flux states, we selected 20 *NuSTAR* pointing of MKN 421, spread over both flaring and non-flaring states. For 10 of these selected epochs, simultaneous *Swift*-XRT observations were available and they are included in this study. This enables us to investigate the source over a broad X-ray energy ranging from 0.3 to 79keV. The details of these observations are given in Table 1 and the data reduction techniques used are described below.

2.1 *Nu STAR*

NuSTAR is a space-based focusing high energy X-ray telescope, consisting of two co-aligned, independent telescopes; FPMA and FPMB (Focal Plane Module A and B) for parallel observations (Harrison et al. 2013). It operates in the hard X-ray energy band from 3 to 79 keV with subarcmin angular resolution and provides a more than 100-fold improvement in sensitivity beyond 10 keV over other telescopes. *NuSTAR* archival data were obtained from NASA'S HEASARC interface[1] and the data were reduced using the NUSTARDAS software package (Version 1.4.1) built in HEASOFT (Version 6.19). A circular region of radius 30 arcsec and centred around the source is used to extract the source spectrum and the background is estimated from a circular region of radius 50 arcsec free from source contamination but adjacent to it. With these selections of source and background regions, the NUPRODUCT (Version 0.2.8) script was used to produce the spectrum for each observation.[2] Finally, the clean event files, ancillary response files (ARFs) and response matrices (RMF) were generated using the standard NUPIPELINE (Version 0.4.5). The source spectrum for FPMA and FPMB were then grouped individually using the GRPPHA tool to have a minimum of 30 counts bin^{-1}. This ensures χ^2 statistics will remain valid during spectral fitting using XSPEC (Arnaud 1996).

2.2 *Swift*-XRT

The *Swift*-XRT (Burrows et al. 2005) observations are obtained from NASA'S HEASARC interface and the data reduced using the XRTDAS software package (Version 3.0.0) built-in HEASOFT. The observations were made in Windowed Timing (WT) mode and standard procedures followed to calibrate and generate the cleaned event files

[1] https://heasarc.gsfc.nasa.gov/
[2] https://heasarc.gsfc.nasa.gov/docs/nustar/analysis/

Table 1. Details of *NuSTAR* observations for 20 different pointings and the simultaneous *Swift*-XRT observations.

Obs.	*NuSTAR*			*Swift*-XRT		
	Obs. ID	Obs. date and time (yy-mm-dd)	Exposure (s)	Obs. ID	Obs. date and time (yy-mm-dd)	Exposure (s)
s1	10002015001	2012-07-07 T01:56:07	42034	–	–	–
s2	10002016001	2012-07-08 T01:46:07	24885	–	–	–
s3	60002023006	2013-01-15 T00:56:07	24182	–	–	–
s4	60002023010	2013-02-06 T00:16:07	19307	–	–	–
s5	60002023012	2013-02-12 T00:16:07	14780	–	–	–
s6	60002023014	2013-02-16 T23:36:07	17359	00080050006	2013-02-17 T00:03:59	9201
s7	60002023016	2013-03-04 T23:06:07	17252	00080050007	2013-03-04 T23:34:25	984
s8	60002023018	2013-03-11 T23:01:07	17474	00080050011	2013-03-11 T23:58:59	8425
s9	60002023020	2013-03-17 T00:11:07	16558	–	–	–
s10	60002023022	2013-04-02 T17:16:07	24772	–	–	–
s11	60002023024	2013-04-10 T21:26:07	5758	–	–	–
s12	60002023025	2013-04-11 T01:01:07	57509	00080050016	2013-04-11 T00:30:59	1076
s13	60002023026	2013-04-12 T20:11:07	441	00080050019	2013-04-12 T21:53:58	9546
s14	60002023027	2013-04-12 T20:36:07	7630	00080050019	2013-04-12 T21:53:58	9546
s15	60002023029	2013-04-13 T21:36:07	16510	–	–	–
s16	60002023031	2013-04-14 T21:41:07	15606	–	–	–
s17	60002023033	2013-04-15 T22:01:07	17278	00035014062	2013-04-15 T23:07:59	534
s18	60002023035	2013-04-16 T22:21:07	20279	00035014065	2013-04-17 T00:46:59	8842
s19	60002023037	2013-04-18 T00:16:07	17795	00035014066	2013-04-18 T00:49:59	6887
s20	60002023039	2013-04-19 T00:31:07	15958	00035014067	2013-04-19 T00:52:59	6132

Notes: *NuSTAR* observations of 20 different flux states during 2012 July–2013 April and near simultaneous *Swift*-XRT observations

using XRTPIPELINE (Version 0.13.0).[3] To extract the source spectrum, a circular region of 20 pixels centred at the source is used and for the background, a nearby 40 pixels circular region is selected which is free from the source contamination. In case of observations with pile-up, an annular region with 2 pixels inner boundary and 20 pixels outer boundary is used. The spectrum is produced using XRTPRODUCTS (Version 0.4.2) and the ARFs files and the RMF were generated using XRTMKARF from the *Swift* CALDB. The 0.3–10keV spectra were then grouped as described in the previous section.

2.3 X-ray spectral analysis

We repeat the analysis of Sinha et al. (2015) by fitting the X-ray spectra due to *NuSTAR* and *Swift*-XRT observations of MKN 421 using a log-parabola model, in-built in XSPEC. This will let us to compare the effectiveness of the analytical model given in Section 3 with the empirical one presented here. A log-parabola model is defined as (Massaro et al. 2004a)

$$F(E) = K\left(\frac{E}{E_*}\right)^{-\alpha-\beta\log(E/E_*)}, \quad (1)$$

where, α is the spectral index at energy E_*, β is the curvature parameter, and K is the normalization. Choosing $E_* = 1$ keV, the final spectrum is defined by three parameters α, β, and K. The knowledge of the parameters α and β lets us estimate the peak of the log-parabola function in $E^2F(E)$ representation as

$$\log\left(\frac{E_{\rm p,lp}}{E_*}\right) = \frac{2-\alpha}{2\beta}. \quad (2)$$

The hard X-ray spectra of MKN 421, in the energy range 3–79keV corresponding to 20 observations by *NuSTAR*, is fitted using a log-parabola model and the results are presented in Table 2 (left). The Galactic neutral hydrogen absorption in the direction of MKN 421 is estimated as 1.92×10^{20} cm^{-2} (Kalberla et al. 2005) and fixed throughout the analysis for all the observations. Similar to the earlier results, we found this model can represent the hard X-ray spectra of all the epochs well with a significant curvature (β ranging from 0.14 to 0.49). The hard X-ray spectra mainly reflects the falling part of the synchrotron spectral component and misses the curvature close to the peak. To verify whether the same model is capable of explaining this spectral regime as well, we repeat the spectral fitting by including simultaneous soft X-ray spectra available from *Swift*-XRT observations for 10 epochs (Table 1). We find that the quality of the fits slightly deteriorate, with a significant change in the spectral parameters and in Table 3 (left), we provide the fit results of this combined *Swift*-XRT–*NuSTAR* observations. Interestingly, it can also be noted that the spectral fit is better for the low flux states compared to the high-flux states. In Table 4 (left), we provide the SED peaks obtained using the log-parabola fit parameters corresponding to *NuSTAR* alone and *Swift*-XRT–*NuSTAR* combined spectral fits.

3 ENERGY-DEPENDENT ELECTRON DIFFUSION MODEL

A better understanding of the MKN 421 spectrum and its evolution can be perceived by modelling the X-ray spectra using a physically motivated model rather than a simple empirical function given by equation (1). Accordingly, we consider the electron acceleration and the emission processes in the blazar jet by dividing the main emission zone into two sub regions namely, acceleration region (AR) and cooling region (CR). AR is assumed to be located around a shock front where electrons are accelerated to relativistic energies and diffuse into CR where they lose their energy through radiative processes. Considering a mono-energetic electron injection (Q_o) into the AR, the electron distribution in AR ($n_{\rm ar}$) and CR ($n_{\rm cr}$) after attaining steady state can be described as (Kardashev 1962),

$$\text{AR}: \quad \frac{d}{d\gamma}\left[\left(\frac{\gamma}{\tau_a} - A\gamma^2\right)n_{\rm ar}(\gamma)\right] + \frac{n_{\rm ar}(\gamma)}{\tau_e} = Q_o\delta(\gamma-\gamma_0) \quad (3)$$

[3] http://www.swift.ac.uk/analysis/xrt/index.php

$$\text{CR}: \quad -\frac{d}{d\gamma}\left[B\gamma^2 n_{\rm cr}(\gamma)\right] + \frac{n_{\rm cr}(\gamma)}{t_{\rm e}} = \frac{n_{\rm ar}(\gamma)}{\tau_{\rm e}}, \tag{4}$$

where γ is the dimensionless electron energy ($E = \gamma m_{\rm e}c^2$), $\tau_{\rm a}$ and $\tau_{\rm e}$ is the characteristic electron acceleration and escape time-scales from the AR, $t_{\rm e}$ is the escape time-scale from CR and, $A\gamma^2$ and $B\gamma^2$ determine the radiative energy loss rates in AR and CR happening in the Thomson regime of the scattering process. If we assume a constant $\tau_{\rm a}$ and an energy-dependent $\tau_{\rm e}$ such that their ratio takes the form

$$\frac{\tau_{\rm a}}{\tau_{\rm e}} = \eta_0 \gamma^{\kappa} \tag{5}$$

then the electron distribution in AR will be (Jagan et al. 2018)

$$n_{\rm ar}(\gamma) \propto \gamma^{-1} \exp\left(-\frac{\eta_0}{\kappa}\gamma^{\kappa}\right). \tag{6}$$

Substituting equation (6) in (4), we can obtain the cooled electron distribution in CR as

$$n_{\rm cr}(\gamma) \propto \gamma^{-2} \exp\left(-\frac{\eta_0}{\kappa}\gamma^{\kappa}\right) \quad \text{for} \quad \gamma \gg \frac{1}{\text{Bt}_{\rm e}}. \tag{7}$$

The synchrotron emissivity at photon energy E' due to the electron distribution in CR can be obtained as [4]

$$j_{\rm syn}(E') = \frac{1}{4\pi}\int P_{\rm syn}(\gamma, E')\, n_{\rm cr}(\gamma)\, d\gamma, \tag{8}$$

where, $P_{\rm syn}$ is the single particle synchrotron emissivity (Rybicki & Lightman 1986). Consequently, the flux at the observer can be estimated considering the relativistic Doppler boosting from the blazar jet and cosmological effects as (Begelman, Blandford & Rees 1984; Dermer 1995)

$$F_{\rm syn}(E) = \frac{\delta_{\rm D}^3(1+z)}{d_L^2} V j_{\rm syn}\left(\frac{1+z}{\delta_{\rm D}}E\right), \tag{9}$$

here, $\delta_{\rm D}$ is the jet Doppler factor, z is the redshift of the source, d_L is the luminosity distance, and V is the volume of CR. Approximating $P_{\rm syn}$ as a delta function peaking at

$$E' \rightarrow \gamma^2\left(\frac{heB_{\rm cr}}{2\pi mc}\right),$$

[4] E' is the photon energy measured in CR frame.

Table 2. *NuSTAR* analysis with log-parabola and energy-dependent electron diffusion models.

Obs.	Log-parabola			Energy-dependent electron diffusion			$F_{3-10\,\rm keV}$
	α	β	$\chi^2_{\rm red}$(dof)	ξ_0	κ	$\chi^2_{\rm red}$(dof)	(10^{-10} erg cm^{-2} s^{-1})
s1	2.96 ± 0.01	0.19 ± 0.02	1.09 (801.00)	2.24 ± 0.10	0.22 ± 0.04	1.09 (802.25)	1.05 ± 0.01
s2	2.98 ± 0.01	0.28 ± 0.02	1.21 (796.21)	2.01 ± 0.10	0.33 ± 0.05	1.21 (798.10)	1.16 ± 0.01
s3	3.12 ± 0.01	0.31 ± 0.03	0.95 (529.99)	2.18 ± 0.14	0.34 ± 0.06	0.95 (531.59)	0.77 ± 0.01
s4	3.07 ± 0.01	0.44 ± 0.03	1.01 (575.34)	1.71 ± 0.11	0.52 ± 0.06	1.01 (575.42)	0.99 ± 0.01
s5	2.79 ± 0.01	0.25 ± 0.03	1.01 (588.93)	1.73 ± 0.13	0.34 ± 0.07	1.01 (588.97)	1.13 ± 0.01
s6	3.06 ± 0.02	0.14 ± 0.06	1.05 (438.26)	2.60 ± 0.28	0.15 ± 0.06	1.05 (438.21)	0.44 ± 0.01
s7	3.07 ± 0.01	0.23 ± 0.03	1.04 (578.66)	2.31 ± 0.15	0.26 ± 0.06	1.04 (579.19)	1.14 ± 0.01
s8	3.16 ± 0.01	0.24 ± 0.04	0.96 (484.85)	2.46 ± 0.18	0.26 ± 0.07	0.96 (484.90)	0.87 ± 0.07
s9	2.84 ± 0.01	0.31 ± 0.03	0.99 (581.57)	1.65 ± 0.12	0.41 ± 0.07	0.99 (582.02)	1.16 ± 0.01
s10	2.80 ± 0.01	0.31 ± 0.01	1.04 (933.37)	1.59 ± 0.11	0.42 ± 0.03	1.05 (935.40)	2.82 ± 0.01
s11	3.02 ± 0.01	0.41 ± 0.02	1.02 (628.06)	1.71 ± 0.10	0.49 ± 0.05	1.02 (629.45)	4.25 ± 0.03
s12	2.71 ± 0.01	0.37 ± 0.01	1.04 (1490.75)	1.27 ± 0.02	0.55 ± 0.01	1.04 (1488.23)	6.62 ± 0.01
s13	2.75 ± 0.02	0.49 ± 0.06	1.01 (401.57)	1.09 ± 0.18	0.70 ± 0.05	1.02 (404.32)	11.72 ± 0.12
s14	2.71 ± 0.01	0.46 ± 0.01	0.91 (921.02)	1.03 ± 0.03	0.73 ± 0.02	1.22 (1243.05)	14.05 ± 0.15
s15	2.89 ± 0.01	0.44 ± 0.01	1.00 (910.95)	1.42 ± 0.04	0.57 ± 0.03	1.01 (925.77)	5.27 ± 0.01
s16	2.36 ± 0.01	0.42 ± 0.01	1.06 (1516.55)	0.60 ± 0.01	0.88 ± 0.01	1.03 (1481.27)	14.90 ± 0.18
s17	2.64 ± 0.01	0.35 ± 0.01	0.95 (962.51)	1.20 ± 0.04	0.55 ± 0.03	0.94 (952.79)	5.55 ± 0.01
s18	2.44 ± 0.01	0.36 ± 0.01	1.03 (1206.35)	0.83 ± 0.02	0.69 ± 0.03	1.02 (1203.86)	5.95 ± 0.02
s19	2.94 ± 0.01	0.40 ± 0.03	1.01 (566.86)	1.58 ± 0.13	0.51 ± 0.07	1.01 (565.86)	0.96 ± 0.01
s20	3.00 ± 0.01	0.25 ± 0.04	0.90 (467.73)	2.14 ± 0.16	0.29 ± 0.07	0.90 (468.03)	0.90 ± 0.01

Table 3. The combined *Swift*-XRT–*NuSTAR* analysis for 10 epochs using log-parabola and energy-dependent electron diffusion models.

Obs.	Log-parabola			Energy-dependent electron diffusion			$F_{0.3-10\,\rm keV}$
	α	β	$\chi^2_{\rm red}$(dof)	ξ_0	κ	$\chi^2_{\rm red}$(dof)	(10^{-10} erg cm^{-2} s^{-1})
s6	2.57 ± 0.01	0.24 ± 0.01	1.06 (779)	2.14 ± 0.02	0.34 ± 0.01	1.20 (779)	3.41 ± 0.03
s7	2.49 ± 0.03	0.30 ± 0.02	1.04 (760)	2.01 ± 0.05	0.40 ± 0.04	1.05 (760)	7.37 ± 0.17
s8	2.52 ± 0.01	0.32 ± 0.01	1.48 (921)	2.03 ± 0.01	0.45 ± 0.01	1.01 (921)	5.88 ± 0.03
s12	2.20 ± 0.01	0.24 ± 0.01	1.21 (1780)	1.43 ± 0.01	0.44 ± 0.01	1.28 (1780)	17.88 ± 0.19
s13	1.92 ± 0.03	0.34 ± 0.01	1.41 (903)	0.86 ± 0.01	0.88 ± 0.03	1.22 (903)	42.02 ± 1.04
s14	1.90 ± 0.01	0.39 ± 0.01	1.34 (1519)	0.89 ± 0.01	0.86 ± 0.01	1.30 (1519)	41.86 ± 0.27
s17	2.04 ± 0.01	0.29 ± 0.01	1.02 (1309)	1.18 ± 0.03	0.56 ± 0.02	0.98 (1309)	16.85 ± 0.23
s18	1.90 ± 0.02	0.25 ± 0.01	1.53 (1733)	0.83 ± 0.01	0.69 ± 0.01	1.28 (1733)	17.93 ± 0.12
s19	2.42 ± 0.01	0.22 ± 0.01	1.13 (996)	1.18 ± 0.01	0.35 ± 0.01	1.09 (996)	5.83 ± 0.31
s20	2.48 ± 0.05	0.25 ± 0.01	1.01 (931)	1.96 ± 0.01	0.37 ± 0.01	1.05 (931)	6.40 ± 0.64

Table 4. The estimated SED peaks, E_p with the combined XRT–*NuSTAR* (0.3–79 keV), and *NuSTAR* (3–79keV) observations using log-parabola and energy-dependent electron diffusion models.

Obs.	$E_{p,\,lp}$ (keV)		$E_{p,\,esc}$ (keV)	
	XRT–*NuSTAR*	*Nu*STAR	XRT–*NuSTAR*	*NuSTAR*
s6	0.06 ± 0.01	0.003 ± 0.05	0.01 ± 0.01	1.15e−5± 0.001
s7	0.15 ± 0.04	0.05 ± 0.09	0.03 ± 0.01	7.66e−4± 0.01
s8	0.16 ± 0.01	0.04 ± 0.08	0.04 ± 0.01	1.05e−3± 0.01
s12	0.38 ± 0.02	1.11 ± 0.05	0.19 ± 0.01	0.41 ± 0.03
s13	1.27 ± 0.04	1.73 ± 0.50	1.42 ± 0.04	0.77 ± 0.39
s14	1.33 ± 0.03	1.88 ± 0.10	1.26 ± 0.05	0.91 ± 0.08
s17	0.84 ± 0.07	1.20 ± 0.13	0.54 ± 0.06	0.51 ± 0.08
s18	1.51 ± 0.03	2.48 ± 0.13	1.69 ± 0.04	1.67 ± 0.15
s19	0.11 ± 0.01	0.68 ± 0.23	0.03 ± 0.01	0.16 ± 0.10
s20	0.12 ± 0.01	0.10 ± 0.13	0.02 ± 0.01	0.06 ± 0.01

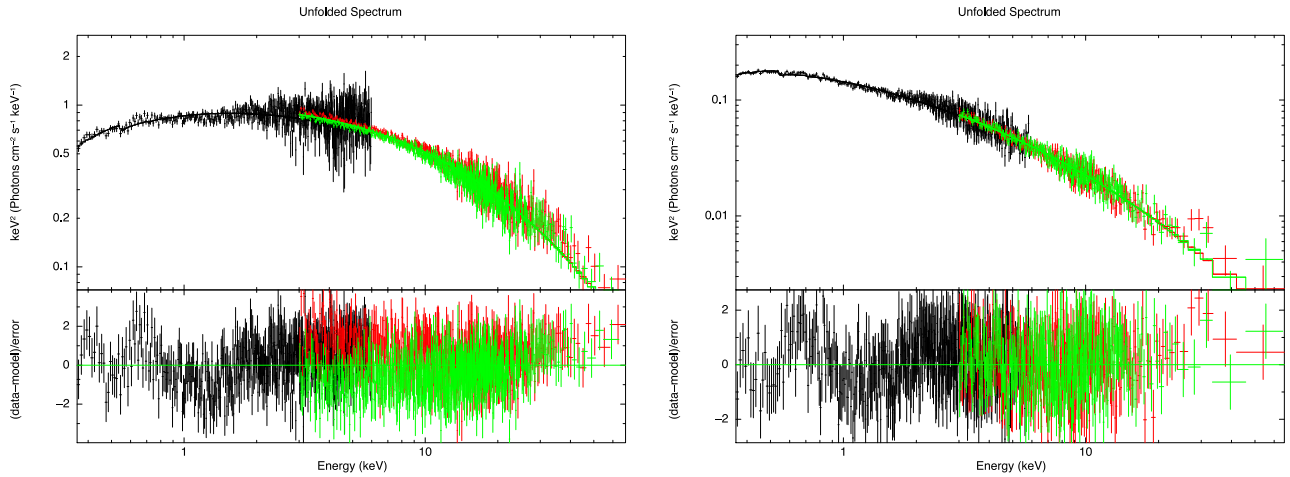

Figure 1. Spectral fit with simultaneous *Swift*-XRT (black) and *NuSTAR* (FPMA: red and FPMB: green) observations correspond to high-flux s14(LHS) and low-flux s8(RHS) state observations using our energy-dependent electron diffusion model.

the observed synchrotron flux can be expressed as (Shu 1991; Sahayanathan, Sinha & Misra 2018).

$$F_{\rm syn}(E) \propto E^{-3/2} \exp\left(-\frac{\xi_0}{\kappa}\,{\rm E}^{\kappa/2}\right), \tag{10}$$

here $B_{\rm cr}$ is the magnetic field of the CR, h is the Planck constant, e electron charge, m electron rest mass and c is the velocity of light. We parameterize the relation between the observed photon energy with the corresponding electron energy through ξ_0 which is given by

$$\xi_0 = \eta_0 \left[\frac{\delta_{\rm D} h e B_{\rm cr}}{2(1+z)\pi mc}\right]^{-\kappa/2}. \tag{11}$$

From equation (10), it is evident the observed synchrotron spectral shape is governed by the parameters ξ_0 and κ and hence, the number of free parameters are equal to the case of log-parabola function. This enables us to perform a detailed comparison between these two models based on their X-ray spectral fit results. The peak of the synchrotron spectrum, given by equation (10), in $E^2F_{\rm syn}(E)$ representation will be

$$E_{\rm p,esc} = \left(\frac{1}{\xi_0}\right)^{2/\kappa} \tag{12}$$

Alternatively, in terms of $E_{\rm p,\,esc}$ equation (10) can be expressed as

$$F_{\rm syn}(E) \propto E^{-3/2} \exp\left[-\frac{1}{\kappa}\left(\frac{\rm E}{\rm E_{p,esc}}\right)^{\kappa/2}\right]. \tag{13}$$

It can be shown that equation (10) will be similar to a log-parabola function for $\kappa \ll 1$ with the parameters related as

$$\alpha \approx \tfrac{1}{2}[3 + \xi_0(1 - 2.303\,\kappa \log E_*)] \tag{14}$$

$$\beta \approx 2.303\,\tfrac{\xi_0\,\kappa}{4}. \tag{15}$$

We refit the *NuSTAR* and *Swift*-XRT observations of MKN 421 by adding equation (10) as a local model in XSPEC. Similar to the log-parabola model, the 20 hard X-ray observations by *NuSTAR* in the energy range 3–79keV can be well fitted by this model. In Table 2 (right), we provide the best-fitting parameters for these observations and the $\chi^2_{\rm red}$ are comparable with the log-parabola model. However, a marginal improvement in the spectral fit compared to a log-parabola model is obtained for the 10 simultaneous observations by *Swift*-XRT and *NuSTAR*. In Table 3 (right), we provide the best-fitting parameters for the combined *Swift*-XRT–*NuSTAR* observations along with the $\chi^2_{\rm red}$ values and in Fig. 1, we show the broad X-ray spectral fit for high-flux state s14 (LHS) and low flux state s8 (RHS). Similar to the log-parabola spectral fit, the best-fitting parameters for this case differ considerably from the fitting of the *NuSTAR* observation alone. Nevertheless, the fit is better for

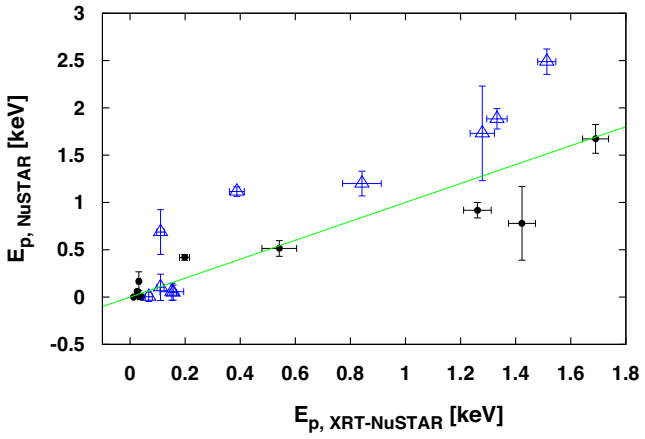

Figure 2. The plot between SED peaks estimated from the fit parameters corresponding to *NuSTAR* observations alone and the combined *Swift*-XRT and *NuSTAR* observations. Blue triangles correspond to the log-parabola model and black circles correspond to the energy-dependent electron diffusion model. The identity line is shown in green.

the high-flux states compared to the log-parabola model. In Table 4 (right), we provide the SED peaks obtained using the fit parameters corresponding to *NuSTAR* alone and *Swift*-XRT–*NuSTAR* combined spectral fits and their distribution is shown in Fig. 2 (black circles) along with an identity line for comparison. It can be seen that the distribution is closer to the identity line compared to the case of log-parabola fit, suggesting the peak estimation is better in the present case. Hence, it can be contemplated that the functional form given by equation (10) may represent the broad-band SED of MKN 421 better than the log-parabola function, though it requires further detailed study to assert this.

To study the dependence between the fit parameters and also with the observed properties, we perform a Spearman rank correlation study among these quantities for the case of log-parabola and the energy-dependent electron diffusion model. In Table 5, we provide the correlation results where the top rows correspond to log-parabola model and the bottom ones belong to energy-dependent electron diffusion model. The scatter plots between the energy-dependent electron diffusion model parameters and the estimated flux are shown in Fig. 3. A strong anticorrelation is observed between ξ_0 and $F_{3-10\,\mathrm{keV}}$ with $r_s = -0.82$ ($p_{rs} = 9.86 \times 10^{-6}$) and a similar correlation is also obtained for the case of log-parabola parameter α with the correlation coefficient $r_s = -0.8$ (null probability hypothesis $p_{rs} = 3.92 \times 10^{-5}$). The latter correlation reflects the 'Harder when brighter' trend of the source which is consistent

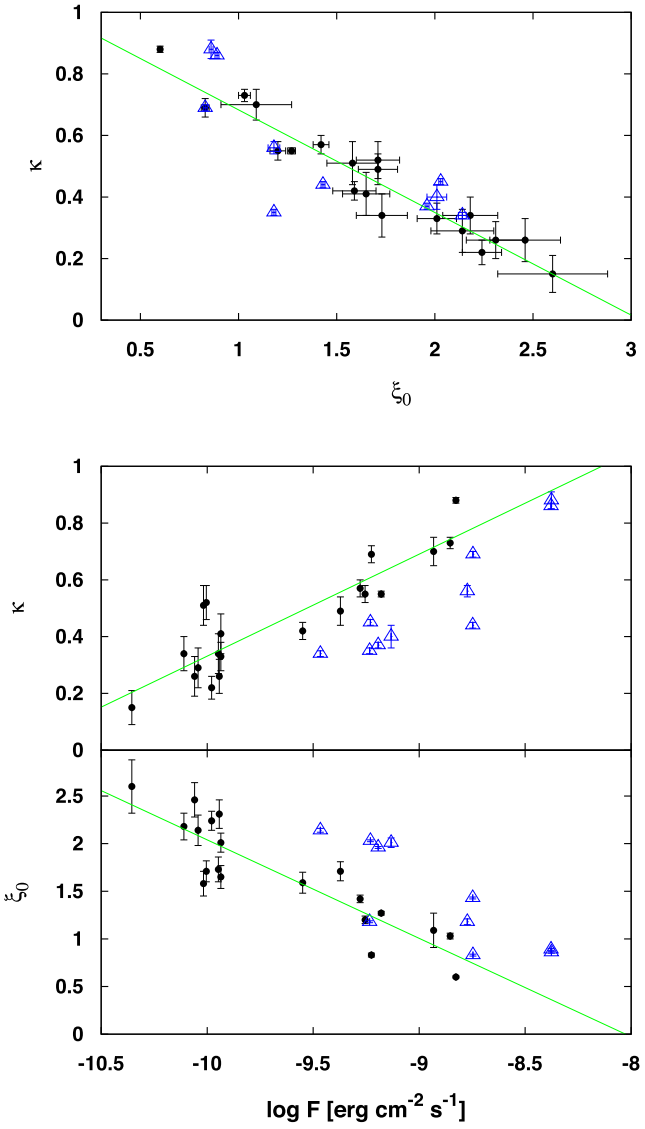

Figure 3. Scatter plot between the energy-dependent electron diffusion model parameters: ξ_0, κ, and the average flux in the range 3 –10keV and 0.3 –10keV for two different sets of observations. The black circles correspond to *NuSTAR* observations alone and the blue triangles correspond to the combined *Swift*-XRT–*NuSTAR* observations. The solid green lines represent the best fit for *Nu*STAR observations.

Table 5. Spearman rank correlation results between the model parameters and the observable quantities for log-parabola and energy-dependent electron diffusion model with the *NuSTAR* observations.

Model	Correlations	r_s	p_{rs}
Log-parabola	β versus $F_{3-10\,\mathrm{keV}}$	0.61	4.0×10^{-3}
	α versus $F_{3-10\,\mathrm{keV}}$	−0.80	3.92×10^{-5}
	β versus α	−0.39	9.70×10^{-3}
	$E_{p,\,lp}$ versus $F_{0.3-10\,\mathrm{keV}}$	0.89	4.91×10^{-4}
Energy dependent electron diffusion	κ versus $F_{3-10\,\mathrm{keV}}$	0.80	2.66×10^{-5}
	ξ_0 versus $F_{3-10\,\mathrm{keV}}$	−0.82	9.86×10^{-6}
	κ versus ξ_0	−0.96	1.50×10^{-11}
	$E_{p,\,esc}$ versus $F_{0.3-10\,\mathrm{keV}}$	0.89	5.40×10^{-4}

Notes: E_p and $F_{0.3-10\,\mathrm{keV}}$ are estimated for the combined *Swift*-XRT and *Nu*STAR observations respectively. Here, r_s is the rank co-efficient and p_{rs} denotes the null hypothesis probability.

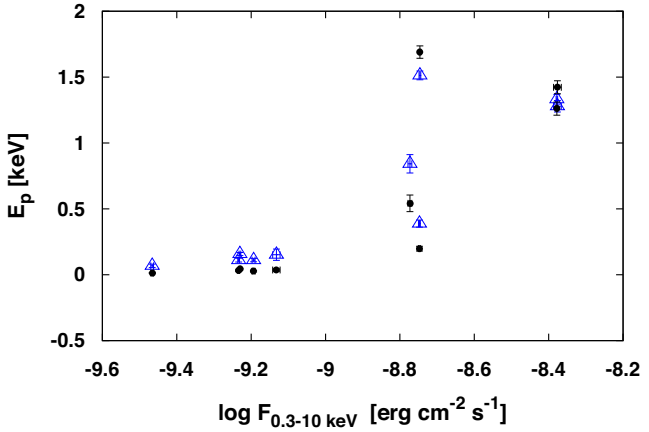

Figure 4. The plot between SED peak and 0.3 –10keV flux for the combined *Swift*-XRT and *NuSTAR* observations estimated from log-parabola model (blue triangles) and the energy-dependent electron diffusion model (black circles).

with the earlier studies (Sinha et al. 2015). The similarity of the correlation between ξ_0 and α is expected since they are closely related through equation (14), particularly for small value of κ. The study between κ and $F_{3-10\,\mathrm{keV}}$ showed a strong correlation with $r_s = 0.8$ ($p_{rs} = 2.66 \times 10^{-5}$), suggesting that the energy dependence of the escape time-scale to increase at high-flux states. On the contrary, the correlation between β of the log-parabola model and the $F_{3-10\,\mathrm{keV}}$ is moderate with $r_s = 0.61$ ($p_{rs} = 4 \times 10^{-3}$). Notably, a strong anticorrelation is seen between the fit parameters ξ_0 and κ with $r_s = -0.96$ ($p_{rs} = 1.5 \times 10^{-11}$) and this was not the case with the parameters α and β of the log-parabola model where we obtained a poor correlation with $r_s = -0.39$ ($p_{rs} = 9.7 \times 10^{3}$). The lack of significant correlation between the log-parabola parameters also suggest that the spectral evolution cannot be attributed to the energy dependence of the particle acceleration process proposed in Massaro et al. (2004a). These correlation studies further hint that the functional form given by equation (10) may probably give a better understanding regarding the emission processes in blazars.

4 SUMMARY AND DISCUSSION

In this work, we perform a detailed X-ray spectral study of the blazar MKN 421 using *NuSTAR* and *Swift*-XRT observations. In addition to modelling the X-ray spectra using a simple log-parabola, we use a physical model involving acceleration of electrons and subsequent emission through synchrotron radiation. The escape of electrons from the main AR is assumed to be energy dependent and we found the synchrotron spectrum due to this physical model can imitate the curved spectra. We show for 20 epochs of *NuSTAR* observation, a log-parabola as well as the energy-dependent electron diffusion models are capable to explain the data very well. However, for 10 epochs with simultaneous *Swift*-XRT observations, the energy-dependent electron diffusion model is marginally favoured than the log-parabola. Moreover, the peak of the SED estimated from the best-fitting parameters for the combined *Swift*-XRT–*NuSTAR* and lone *NuSTAR* observations closely satisfy the identity line in case of energy-dependent electron diffusion model compared to the log-parabola model. This suggests that the functional form obtained from the energy-dependent electron diffusion model, equation (10), may be capable of representing broad-band SED better than the log-parabola model. Further, the correlation studies indicate that the fit parameters of the energy-dependent electron diffusion model are well correlated during various epochs and hence this model is capable of deciphering the electron diffusion process in blazar jets.

The SED peaks estimated using the log-parabola and the energy-dependent electron diffusion models, $E_{p,\,lp}$ and $E_{p,\,esc}$, through the combined *Swift*-XRT–*Nu*STAR observations are only representative since they sometimes fall at energies lower than the X-ray energy range considered here. However, they can be used to identify the trend of peak shifts during various flux states. We computed the Spearman rank correlation between the two estimated spectral peaks and the 0.3–10keV integrated flux ($F_{0.3-10\,\mathrm{keV}}$). The results are shown in Table 5 and the scatter plot between the peaks and $F_{0.3-10\,\mathrm{keV}}$ are shown in Fig. 4. We find both $E_{p,\,lp}$ and $E_{p,\,esc}$ correlate well with $F_{0.3-10\,\mathrm{keV}}$. The observed positive correlation suggests, the SED peak shifts towards higher energies during the higher flux states. However, this inference needs to be verified with the information at lower energies.

The analytical solution of the energy-dependent electron diffusion model used in this work corresponds to the radiatively cooled regime of the electron distribution where $\gamma \gg (B\,t_e)^{-1}$. This prevents us from extending the current model to UV/optical energies where the corresponding electron energies may not satisfy this condition. Alternatively, a semi-analytical solution to equation (4) can be obtained which will be valid even beyond energies imposed by this condition as well as at the SED peak. However, inclusion of such a model into XSPEC will be rigorous and will be carried out in the future work. A successful implementation of this will be effective in constraining $E_{p,\,esc}$ and can verify the results discussed above. The observational periods of *NuSTAR* and *Swift*-XRT considered here overlaps partially and are not strictly simultaneous (Table 1). This can introduce a substantial uncertainty in the estimated parameters owing to the rapid spectral evolution of the source. In this regard, a true simultaneous observation at energies ranging from UV to hard X-ray bands can be obtained from the multiwavelength satellite-based experiment, *ASTROSAT* which can resolve this discrepancy.

The observed strong anticorrelation between the parameters of the energy-dependent electron diffusion model, ξ_0 and κ, suggests these quantities may be dependent on each other. The dependence of ξ_0 on κ is evident from equation (11) where the latter, besides depending on the physical parameters of the source, is also a function of κ. On the contrary, if these parameters were found to be uncorrelated, then it could have been a sufficient condition to reject the proposed model. Nevertheless, the observed correlation is still not sufficient enough to validate the assumed model unless the correlation is tested with the choice of parameters that can be shown independently. This demands a prior information about the physical parameters of the source (e.g. source magnetic field, jet Lorentz factor, etc.) which cannot be estimated from the narrow band of SED considered here. These pieces of information can be obtained through broad-band spectral modelling of the source from radio to γ-ray using a numerical solution of the equation (4) and incorporating full synchrotron and inverse Compton emission processes, which will be pursued in the future.

ACKNOWLEDGEMENTS

We thank the anonymous referee for insightful comments and constructive suggestions. This research has made use of data, software, and/or web tools obtained from NASAs High Energy Astrophysics Science Archive Research Center (HEASARC), a service of the God-

dard Space Flight Center and the Smithsonian Astrophysical Observatory. This research has made use of the XRT Data Analysis Software (XRTDAS) and the NuSTAR Data Analysis Software (NUSTARDAS) jointly developed by the ASI Science Data Center (ASDC, Italy) and the California Institute of Technology (Caltech, USA). PG would like to thank IUCAA and BARC for their hospitality. RG would like to thank the IUCAA associateship programme and CSIR, New Delhi (03(1412)/17/EMR-II) for the financial support.

REFERENCES

Abdo A. A. et al., 2011, ApJ, 736, 131
Acciari V. A. et al., 2009, ApJ, 703, 169
Aleksić J. et al., 2012, A&A, 542, A100
Arnaud K. A., 1996, in Jacoby G. H., Barnes J., eds, ASP Conf. Ser. Vol. 101, Astronomical Data Analysis Software and Systems V, Astron. Soc. Pac. , San Francisco, p. 17
Bartoli B. et al., 2016, ApJS, 222, 6
Begelman M. C., Blandford R. D., Rees M. J., 1984, RvMP, 56, 255
Bhagwan J., Gupta A. C., Papadakis I. E., Wiita P. J., 2014, MNRAS, 444, 3647
Burrows D. N. et al., 2005, Science, 309, 1833
Chen L., 2014, ApJ, 788, 179
Dermer C. D., 1995, ApJ, 446, L63
Donnarumma I. et al., 2009, ApJ, 691, L13
Fossati G. et al., 2000, ApJ, 541, 166
Gaur H., Chen L., Misra R., Sahayanathan S., Gu M. F., Kushwaha P., Dewangan G. C., 2017, ApJ, 850, 209
Harrison F. A. et al., 2013, ApJ, 770, 103
Jagan S. K., Sahayanathan S., Misra R., Ravikumar C. D., Jeena K., 2018, MNRAS, 478, L105
Kalberla P. M. W., Burton W. B., Hartmann D., Arnal E. M., Bajaja E., Morras R., Pöppel W. G. L., 2005, A&A, 440, 775
Kapanadze B., Romano P., Vercellone S., Kapanadze S., 2014, MNRAS, 444, 1077
Kapanadze B. et al., 2016, ApJ, 831, 102
Kardashev N. S., 1962, SvA, 6, 317
Kataoka J., Stawarz Ł., 2016, ApJ, 827, 55
Landau R. et al., 1986, ApJ, 308, 78
Massaro E., Perri M., Giommi P., Nesci R., 2004a, A&A, 413, 489
Massaro E., Perri M., Giommi P., Nesci R., Verrecchia F., 2004b, A&A, 422, 103
Massaro E., Tramacere A., Perri M., Giommi P., Tosti G., 2006, A&A, 448, 861
Massaro F., Tramacere A., Cavaliere A., Perri M., Giommi P., 2008, A&A, 478, 395
Padovani P., Giommi P., 1995, ApJ, 444, 567
Paggi A., Massaro F., Vittorini V., Cavaliere A., D'Ammando F., Vagnetti F., Tavani M., 2009, A&A, 504, 821
Rybicki G. B., Lightman A. P., 1986, Radiative Processes in Astrophysics, Revised edition (March 26, 1985), Wiley-VCH
Sahayanathan S., Sinha A., Misra R., 2018, RAA, 18, 35
Sambruna R. M., Barr P., Giommi P., Maraschi L., Tagliaferri G., Treves A., 1994, ApJS, 95, 371
Shu F. H., 1991, Radiation: The Physics of Astrophysics, Vol. 1, University Science Books, Mill Valley, CA, USA
Sinha A., Shukla A., Misra R., Chitnis V. R., Rao A. R., Acharya B. S., 2015, A&A, 580, A100
Sinha A. et al., 2016, A&A, 591, A83
Sinha A., Sahayanathan S., Acharya B. S., Anupama G. C., Chitnis V. R., Singh B. B., 2017, ApJ, 836, 83
Tavecchio F., Maraschi L., Ghisellini G., 1998, ApJ, 509, 608
Tramacere A. et al., 2007, A&A, 467, 501
Tramacere A., Giommi P., Perri M., Verrecchia F., Tosti G., 2009, A&A, 501, 879
Yan D., Zhang L., Yuan Q., Fan Z., Zeng H., 2013, ApJ, 765, 122
Zhu Q., Yan D., Zhang P., Yin Q.-Q., Zhang L., Zhang S.-N., 2016, MNRAS, 463, 4481

This paper has been typeset from a TEX/LATEX file prepared by the author.